Observations of seasonal upwelling and downwelling in the Beaufort Sea mediated by sea ice

Gianluca Meneghello*

Department of Earth, Atmospheric and Planetary Sciences, Massachusetts Institute of Technology, Cambridge, Massachusetts 02139-4307, USA.

John Marshall

Department of Earth, Atmospheric and Planetary Sciences, Massachusetts Institute of Technology, Cambridge, Massachusetts 02139-4307, USA.

Mary-Louise Timmermans

Department of Geology and Geophysics, Yale University, New Haven, Connecticut, USA

Jeffery Scott

Department of Earth, Atmospheric and Planetary Sciences, Massachusetts Institute of Technology, Cambridge, Massachusetts 02139-4307, USA.

**Corresponding author address:* Department of Earth, Atmospheric and Planetary Sciences, Massachusetts Institute of Technology, Cambridge, Massachusetts 02139-4307, USA.

E-mail: gianluca.meneghello@gmail.com

ABSTRACT

We present observational estimates of Ekman pumping in the Beaufort Gyre region. Averaged over the Canada Basin, our results show a 2003-2012 average of $2.5\,\mathrm{m\,yr^{-1}}$ downward with strong seasonal and interannual variability superimposed: monthly and yearly means range from $30\,\mathrm{m\,yr^{-1}}$ downward to $10\,\mathrm{m\,yr^{-1}}$ upward. A clear seasonal cycle is evident with intense downwelling in autumn and upwelling during the winter months. Wintertime upwelling is associated with friction between the large scale Beaufort Gyre ocean circulation and the surface ice pack, and contrasts with previous estimates of year-long downwelling; as a consequence, the yearly cumulative Ekman pumping over the gyre is significantly reduced. The spatial distribution of Ekman pumping is modified as well, with the Beaufort Gyre region showing alternating, moderate upwelling and downwelling, while a more intense, year-long downwelling averaging $17.5\,\mathrm{m\,yr^{-1}}$ is identified in the northern Chukchi Sea region. Implications of our results for understanding Arctic Ocean dynamics and change are discussed.

1. Introduction

Ekman pumping plays a central role in the generation and maintenance of the Beaufort Gyre, the largest freshwater reservoir in the Arctic (Proshutinsky et al. 2009). The pumping rates depend on the stress acting at the surface due to the wind in the open ocean and to the stress imparted to the ocean by ice, itself driven by the wind, in regions of ice cover.

Most estimates of Ekman pumping assume that surface ocean geostrophic currents can be neglected (Yang 2006, 2009) or focus on the summer season when ice can be considered in free drift (McPhee 2013). The resulting Ekman pumping field, driven by anticyclonic winds and ice drift associated with the highly variable but persistent high pressure system over the Beaufort region, is characterized by year-long downwelling, modulated by a seasonal cycle in intensity but not in sign (Proshutinsky et al. 2009). As a consequence, it is assumed that the gyre is continuously inflated with freshwater, which can be released by baroclinic instability generated eddies (Manucharyan and Spall 2016; Manucharyan et al. 2016; Meneghello et al. 2017) or other mechanisms. The limit case in which Ekman pumping is exactly balanced by eddy induced upwelling is exploited in Meneghello et al. (2017) to place a constraint on the magnitude of the mesoscale eddy diffusivity.

Hydrographic and satellite-based observations suggest that surface geostrophic currents have increased dramatically over the past decade, consistent with the observed increase of freshwater content in the Beaufort Gyre region (Proshutinsky et al. 2009; McPhee 2013) or the equivalent doming of the dynamic ocean topography or geopotential height (Armitage et al. 2016, 2017). Geostrophic currents of the order of 2 to $4\,\mathrm{cm\,s^{-1}}$ cannot be neglected compared to ice velocities of order 5 to $10\,\mathrm{cm\,s^{-1}}$. This is particularly true during winter in regions where internal ice stresses prevent the pack from freely moving in response to wind forcing. In this case, friction between the anticyclonic surface ocean geostrophic flow and a relatively stationary sea-ice pack gives rise to upwelling (in opposition to downwelling that would arise for the same wind forcing in the absence of sea ice).

Numerical studies (Martin and Gerdes 2007; Martin et al. 2014, 2016) implicitly take into account the surface ocean current, but have not emphasized the implications for the Ekman pumping field itself or teased apart the controlling processes. Instead they often focus on characterization of sea-ice drift, the surface stress and the effect of varying drag coefficients.

Using observational datasets, we first showed in Meneghello et al. (2017) how the inclusion of the interaction between the ice and the geostrophic current associated with the Beaufort Gyre significantly changes the annual mean Ekman pumping. A detailed analysis of the updated Ekman pumping is the focus of the current study.

In this paper, we analyze observations spanning the period 2003 to 2012 to discern how the complex relationships between winds, a temporally and spatially varying sea-ice pack, and surface ocean geostrophic flows influence Ekman upwelling and downwelling in the central Beaufort Gyre Region and margins. In previous studies (Yang 2006, 2009; McPhee 2013) the central gyre has been discussed in a broad sense without regard for topographic boundaries; the essential dynamics at its margins are often ignored. Here we further explore the significant regional patterns of the Ekman pumping field and describe their importance to the gyre as a whole.

The paper is organized as follows. We begin in §2 by outlining the methods used to compute Ekman pumping rates; our approach is similar to the one used by Yang (2006, 2009), with the main difference being the addition of the geostrophic current introduced in Meneghello et al. (2017). In §3 we present estimates of the Ekman pumping field; we plot time series of Ekman pumping averaged over the Beaufort Gyre Region (BGR), bounded by 70.5°N to 80.5°N and 130°W to 170°W, and including only regions having depth greater than 300 m (Proshutinsky et al. 2009). We follow in §4 with a discussion of the spatial distribution of Ekman pumping in the BGR, additionally focusing attention on two smaller regions of particular interest in the south of the Canada Basin (BGS) and in the northern Chukchi Sea region (BGC). Results are discussed in §5, where we clarify the effect of the interaction of surface-ocean geostrophic currents with the sea-ice pack and implications to mechanisms controlling the time-dependent buoyancy budget of the Beaufort Gyre in the presence of seasonal sea ice.

2. Methods

Four datasets are combined to estimate the surface ocean stress $\boldsymbol{\tau}$ and Ekman pumping w_{Ek}: (i) sea ice concentration α from Nimbus-7 SMMR and DMSP SSM/I-SSMIS Passive Microwave Data Version 1 (Cavalieri et al. 1996); (ii) sea ice velocity $\boldsymbol{u}_i$ from the Polar Pathfinder Daily 20 km EASE-Grid Sea Ice Motion Vectors, Version 3 (Tschudi et al. 2016); (iii) geostrophic currents $\boldsymbol{u}_g$ computed from Dynamic Ocean Topography (Armitage et al. 2016, 2017) and (iv) 10 m wind $\boldsymbol{u}_a$ from the NCEP-NCAR Reanalysis 1 (Kalnay et al. 1996). The four different datasets, defined on different grids, are interpolated on a common EASE-25 km polar stereographic equal area grid, which is the native grid for the ice velocity. All datasets are available in at least daily resolution, with the exception of dynamic ocean topography having monthly resolution: to produce daily values, we arbitrarily assign the available fields to the 15th of the corresponding month, and linearly interpolate. The 2003-2012 climatology of these four variables is summarized in Figure 1, while variability in time is summarized by their mean values over the BGR (Figure 2a).

The high pressure system at the origin of the gyre is evident in the 10 m wind field (Figure 1a), where the anticyclonic flow is centered at approximately 76°N and 145°W; stronger winds, of order $2.5\,\mathrm{m\,s^{-1}}$, are in the southwestern BGR (the region indicated by a solid black line), while winds are weaker ($\sim 1\,\mathrm{m\,s^{-1}}$ or less) in the northern BGR. Sea-ice drift and surface-ocean geostrophic flow (Figure 1b and c, respectively) also show anticyclonic circulation patterns with strongest speeds ($\sim 5\,\mathrm{cm\,s^{-1}}$) in the southwest, and slowest speeds in the north.

Time series of mean values over the BGR (Figure 2a) indicate a seasonal cycle in the four datasets: ice areal coverage reaches a minimum between 20% and 40% every late summer, with the extreme low (less than 10%) in 2012. Wind speeds tend to peak in late summer/early fall, when sea-ice drift speeds are also fastest. The surface ocean current shows maximum speeds during late fall, peaking at about twice the characteristic speed of the first part of the year; of particular note is its increase in the second part of 2007 (and sustained for several years following).

Starting from the four datasets described above, we use the same approach used in Meneghello et al. (2017) and compute the daily surface-ocean stress $\boldsymbol{\tau}$ as a combination of ice-ocean and air-ocean surface stresses, each estimated using a quadratic drag law with fixed drag coefficients ($C_{Di} = 0.0055$, $C_{Da} = 0.00125$), and weighted by the observed local ice concentration α:

$$\boldsymbol{\tau} = \alpha \underbrace{\rho C_{Di} \left|\boldsymbol{u}_{rel}\right| (\boldsymbol{u}_{rel})}_{\boldsymbol{\tau}_i} + (1-\alpha) \underbrace{\rho_a C_{Da} \left|\boldsymbol{u}_a\right| (\boldsymbol{u}_a)}_{\boldsymbol{\tau}_a} \tag{1}$$

where the ice-ocean relative velocity $\boldsymbol{u}_{rel}$ may be written in terms of the ice velocity $\boldsymbol{u}_i$, the surface geostrophic velocity $\boldsymbol{u}_g$, and the Ekman velocity $\boldsymbol{u}_e$ as $\boldsymbol{u}_{rel} = \boldsymbol{u}_i - (\boldsymbol{u}_g + \boldsymbol{u}_e)$. The water and air density are taken as $\rho = 1027.5\,\mathrm{kg\,m^{-3}}$ and $\rho_a = 1.25\,\mathrm{kg\,m^{-3}}$ respectively.

Our estimate of the surface ocean current differs from, e.g., Yang (2006, 2009) in two key ways. First, we use the Ekman velocity at the surface (rotated 45° to the right of the surface stress) in place of the mean Ekman transport velocity (90° from the surface stress), thus $\boldsymbol{u}_e = \boldsymbol{\tau}\sqrt{2}e^{-i\frac{\pi}{4}}/(f\rho D_e)$, with $D_e = 20\,\mathrm{m}$ (Yang 2006). Second, and more importantly, we include the surface geostrophic current $\boldsymbol{u}_g$ inferred from dynamic ocean topography (McPhee 2013; Armitage et al. 2016, 2017).

3. Ekman pumping estimates: integral measures

The Ekman pumping rate $w_{Ek} = \nabla \times \boldsymbol{\tau}/(\rho f)$ is computed making use of the daily stress fields obtained as described above, with a Coriolis parameter $f = 1.46 \times 10^{-4}\,\mathrm{s}^{-1}$. We first focus on integral measures averaged over the BGR, summarized in Figure 2b. Over the ten year period 2003-2012, Ekman convergence (solid black curve, negative is downward) results in an average downwelling w_{Ek} of $2.5\,\mathrm{m\,yr}^{-1}$, to be compared with an average of almost $10\,\mathrm{m\,yr}^{-1}$ if the geostrophic current is neglected (dashed black). By comparison, in the scenario of a completely ice free BGR, the wind driven downwelling would be $6.3\,\mathrm{m\,yr}^{-1}$ (solid red).

To better understand the role of the winds, sea-ice and ocean geostrophic currents, we additionally compute the contribution of the geostrophic current to the ice stress as

$$\boldsymbol{\tau}_{ig} = \boldsymbol{\tau}_i - \boldsymbol{\tau}_{i0} \tag{2}$$

where $\boldsymbol{\tau}_{i0}$ is the ice-ocean stress neglecting the geostrophic current, i.e., computed by setting $\boldsymbol{u}_g = 0$ in (1). Accordingly, we define the Ekman pumping associated with each component as

$$\begin{aligned} w_a &= \frac{\nabla \times ((1-\alpha)\boldsymbol{\tau}_a)}{\rho f} \qquad w_i = \frac{\nabla \times (\alpha \boldsymbol{\tau}_i)}{\rho f} \\ w_{i0} &= \frac{\nabla \times (\alpha \boldsymbol{\tau}_{i0})}{\rho f} \qquad w_{ig} = \frac{\nabla \times (\alpha \boldsymbol{\tau}_{ig})}{\rho f} \end{aligned} \tag{3}$$

so that the total Ekman pumping can be written as $w_{Ek} = \frac{\nabla\times\boldsymbol{\tau}}{\rho f} = w_a + w_i = w_a + w_{i0} + w_{ig}$. As a measure of the atmospheric forcing, we additionally define

$$w_A = \frac{\nabla \times \boldsymbol{\tau}_a}{\rho f} \tag{4}$$

as the Ekman pumping that would be realized in a completely ice free BGR.

The area-averaged Ekman pumping time series (30-day running means of daily values, Figure 2b) shows how both the atmospheric forcing w_A (red) and Ekman pumping computed neglecting the geostrophic current $w_a + w_{i0}$ (dotted black) are almost always downwelling-favorable. In contrast the actual pumping w_{Ek} (solid black) has extensive periods of upwelling in the winter each year corresponding to periods when the ice concentration is elevated (gray areas), and strong downwelling in late summer and autumn, when ice concentration is low.

The role of each component in determining the total upwelling or downwelling in the BGR is made clearer in the monthly and yearly area-averages (Figure 3) of w_{Ek} (black bars) and its three components w_a (red bars), w_{i0} and w_{ig} (green and blue bars respectively). We additionally plot w_A (red and white circles), $w_a + w_{i0}$ (red green marks), and the ice concentration (gray circles), as well as the ratio

$$\gamma = \frac{|w_{ig}|}{|w_a| + |w_{i0}| + |w_{ig}|} \tag{5}$$

as a metric of the importance of the geostrophic current relative to the total Ekman pumping (black line).

A seasonal cycle is evident in the monthly climatology of w_{Ek} (black bars, Figure 3a): upwelling in January to March is followed by increasing downwelling over the rest of the year, reaching an October downwelling maximum of slightly more than $10\,\mathrm{m\,yr^{-1}}$, driven by strong wind-stress curl forcing (red and white circles) acting on a largely ice free BGR (gray circles). Downwelling markedly decreases in November and December because of the combined effect of weaker wind-stress curl and high ice concentration. Strong downwelling in the low ice-concentration months of August to October is driven by direct air-ocean wind-stress curl (red bars), and closely follows the hypothetical downwelling result if the BGR was ice free (red and white circles); during these months, the effects of ice and geostrophic currents are relatively minor. During the rest of the year, when ice cover is extensive, direct air-ocean stress plays a minor role and stresses are predominantly mediated by ice cover. The importance of the geostrophic current on the total Ekman pumping, as measured by the ratio γ (equation (5), black line), closely follows the ice concentration: when the BGR is completely ice covered and internal stresses are higher (January to March) the surface ocean geostrophic current is faster than sea-ice drift resulting in net upwelling. Indeed, while the ice effect (green bars) is always downwelling-favorable, the effect of the geostrophic current (blue bars) is consistently upwelling and of the same order of magnitude.

The yearly climatology (Figure 3b) presents a similar range of total Ekman pumping values (black bars) between years, and closely follows the variability of the wind-stress curl acting directly on the ice-free parts of the ocean (red bars), with the ice and geostrophic current effects approximately canceling one-another. Notable exceptions are in 2003 and 2004, when downwelling is mostly driven by ice flowing over a slower geostrophic current, and in 2012, when a fast geostrophic current and cyclonic winds (in the opposite sense to the geostrophic ocean flow) both contribute to upwelling.

4. Ekman pumping estimates: spatial patterns

To better understand the spatial distribution of upwelling and downwelling in the Beaufort Gyre Region we plot monthly and yearly climatological maps of Ekman pumping (Figures 4 and 5, respectively).

We additionally repeat the decomposition of the total Ekman pumping (cf. Figure 3) for two smaller regions: i) the BGC (C for Chukchi), delimited by 72°N and 76°N, 170°W and 160°W, and including only regions shallower than 300 m (thus outside the BGR) and ii) the BGS (S for south), covering the portion of the BGR south of the 72°N parallel (see dashed lines and labels in Figure 1a).

During the first four months of the year (JFMA), a broad region of upwelling is visible in the BGR, particularly towards the southern sector, with local upwelling rates as high as 25 to 30 $\mathrm{m\,yr^{-1}}$ (Figure 4). In the following four months (MJJA), the intensity and extension of the upwelling region decreases; by September, downwelling dominates over most of the BGR. For all months, a marked region of downwelling persists to the southwest of the BGR in the northern Chukchi Sea (in the region we denote BGC). Downwelling in this region intensifies in fall, with October showing downwelling rates in excess of 30 $\mathrm{m\,yr^{-1}}$.

An indication of the role of the geostrophic current in shaping the spatial distribution of Ekman pumping can be inferred by the gray thick line (Figure 4). In the region interior to this line, the geostrophic current reduces the ice driven downwelling, and sometimes gives rise to a net upwelling (i.e., JFM). In contrast, downwelling is enhanced by the presence of the geostrophic current outside of the gray curve (e.g., in the coastal areas and northern sector of the BGR).

Yearly-averaged maps of Ekman pumping (Figure 5) show weak Ekman downwelling and upwelling over most of the BGR. Notable exceptions to this general pattern, as previously noted, are the years 2007 and 2012. In 2007, anomalously strong downwelling extends over most of the BGR (with coastal upwelling in the south) driven by strong (negative) wind-stress curl during a time of low sea-ice extent. In contrast, 2012 is characterized by an extended region of upwelling dominated by summer cyclonic winds in the presence of anomalously low sea-ice extent (see Figure 2b, red curve).

Analysis of the varying distribution of Ekman pumping (Figures 4 and 5) indicates strong, continuous downwelling in the BGC, and strong Ekman pumping of variable sign in the southern part of the BGR (the region denoted BGS).

A detailed analysis of the BGC and BGS regions is provided in Figure 6 and Figure 7 respectively. The BGC region (Figure 6) is characterized by strong, year-long downwelling averaging $17.5\,\mathrm{m\,yr^{-1}}$ over the ten year period. Prevailing easterlies tend to be consistently stronger here compared to anywhere else in the basin (see Figure 1a), and decay towards the north leading to the highest values of horizontal shear and downwelling in this region. The upwelling associated with the positive ice velocity curl (Figure 1c) is offset by the contribution of the ocean geostrophic flow, which is swiftest along the lateral density front approximately coincident with the 100 m isobath (Timmermans et al. 2017) (Figure 1b).

In contrast, in the BGS region (Figure 7) winds and ice velocity increasing in intensity away from the coast results in a 2003-2012 mean upwelling of $2\,\mathrm{m\,yr^{-1}}$. Wind driven downwelling is apparent only in the months of June, July and August, when ice cover is reduced and there is negligible decay of northeasterly winds towards the coast.

It is instructive to compare the relative importance of the total vertical Ekman flux (in this case, upwelling plus downwelling) in each of the different regions, BGR, BGS and BGC.

Table 1 summarizes the surface area, 2003-2012 mean Ekman pumping w_{Ek} and the total corresponding vertical flux for each region. Due to the large downwelling, the vertical flux in the BGC region is approximately 2/3 of that in the BGR, despite the former having only a tenth of the surface area of the latter. We further point out that downwelling in the BGC is sustained (seasonally and interannually) and it has been shown to be a region of key importance for ventilation of the interior Beaufort Gyre (Timmermans et al. 2017).

5. Conclusions and discussion

Observational estimates of Ekman pumping in the BGR show a weak ten-year average Ekman downwelling of the order $-2.5\,\mathrm{m\,yr^{-1}}$, with strong seasonal and interannual variability: monthly and yearly mean Ekman pumping range from $-30\,\mathrm{m\,yr^{-1}}$ to up to $10\,\mathrm{m\,yr^{-1}}$. A clear seasonal cycle is visible: the Beaufort Gyre is driven by upwelling during the winter months and intense downwelling in autumn. Our results contrast with previous estimates showing year-long downwelling (Yang 2006, 2009), and reduce by a factor of four or more the yearly cumulative Ekman pumping in the gyre; the main reason for this difference is our inclusion of the effect of the geostrophic current, which flows in the same direction as the prevailing winds and sea-ice drift. This ocean-ice interaction acts as a strong negative feedback on the response of the gyre to changing winds. Furthermore, we have identified a region of strong, persistent downwelling (the BGC region) which accounts for a significant fraction of the total Ekman transport in the entire Canada Basin. The precise influence of the BGC region on Beaufort Gyre dynamics and stability, and heat and freshwater content, remains to be tested.

In the larger BGR, the seasonal alternation of wind-driven downwelling and geostrophic current driven upwelling suggests a new possible mechanism in the regulation of Beaufort Gyre intensity.

Recent numerical and observational studies (Manucharyan and Spall 2016; Manucharyan et al. 2016, 2017; Meneghello et al. 2017), analyze the Beaufort Gyre under two assumptions: persistent downwelling and a steady state. In this framework, an intense baroclinic eddy field is required to limit the gyre spin-up (steepening of the isopycnals) and release the freshwater accumulated in the gyre. Horizontal eddy diffusivity estimates for the Beaufort Gyre are around $K \approx 500\,\mathrm{m^2\,s^{-1}}$ (Manucharyan and Spall 2016; Manucharyan et al. 2016; Meneghello et al. 2017), suggesting freshwater release takes place on a diffusive time scale of $L^2/K \approx 15\,\mathrm{yr}$ for a characteristic lateral gyre scale $L = 500\,\mathrm{km}$.

Our results here suggest on the other hand that the release of freshwater is at least partially mediated by winter Ekman upwelling. More research is required to discern the interplay between freshwater release by baroclinic instability versus deflation induced by surface ocean-ice frictional processes, and to better define the characteristic time scales of the latter. This will be the subject of a follow-up paper.

Acknowledgment. We thank Jean-Michel Campin, Edward Dorridge and James Williams for their help and insights. The experiments described here were made possible by support from the NSF program in Arctic Research, Award Number 1603557.

References

Armitage, T. W. K., Bacon, S., Ridout, A. L., Petty, A. A., Wolbach, S., and Tsamados, M. (2017). Arctic Ocean geostrophic circulation 2003-2014. *The Cryosphere Discussions*, 2017:1–32.

Armitage, T. W. K., Bacon, S., Ridout, A. L., Thomas, S. F., Aksenov, Y., and Wingham, D. J. (2016). Arctic sea surface height variability and change from satellite radar altimetry and GRACE, 2003-2014. *Journal of Geophysical Research: Oceans*, 121(6):4303–4322.

Cavalieri, D. J., Parkinson, C. L., Gloersen, P., and Zwally, H. J. (1996). Sea Ice Concentrations from Nimbus-7 SMMR and DMSP SSM/I-SSMIS Passive Microwave Data, Version 1.

Kalnay, E., Kanamitsu, M., Kistler, R., Collins, W., Deaven, D., Gandin, L., Iredell, M., Saha, S., White, G., Woollen, J., Zhu, Y., Chelliah, M., Ebisuzaki, W., Higgins, W., Janowiak, J., Mo, K. C., Ropelewski, C., Wang, J., Leetmaa, A., Reynolds, R., Jenne, R., and Joseph, D. (1996). The NCEP/NCAR 40-year reanalysis project. *Bulletin of the American Meteorological Society*, 77(3):437–471.

Manucharyan, G. E. and Spall, M. A. (2016). Wind-driven freshwater buildup and release in the Beaufort Gyre constrained by mesoscale eddies. *Geophysical Research Letters*.

Manucharyan, G. E., Spall, M. A., and Thompson, A. F. (2016). A Theory of the Wind-Driven Beaufort Gyre Variability. *Journal of Physical Oceanography*, (2013):3263–3278.

Manucharyan, G. E., Thompson, A. F., and Spall, M. A. (2017). Eddy Memory Mode of Multidecadal Variability in Residual-Mean Ocean Circulations with Application to the Beaufort Gyre. *Journal of Physical Oceanography*, 47(4):855–866.

Martin, T. and Gerdes, R. (2007). Sea ice drift variability in Arctic Ocean Model Intercomparison Project models and observations. *Journal of Geophysical Research*, 112(C4):C04S10.

Martin, T., Steele, M., and Zhang, J. (2014). Seasonality and long-term trend of Arctic Ocean surface stress in a model. *Journal of Geophysical Research : Oceans*, (1):1723–1738.

Martin, T., Tsamados, M., Schroeder, D., and Feltham, D. (2016). The impact of variable sea ice roughness on changes in Arctic Ocean surface stress: A model study. *Journal of Geophysical Research - Oceans*, pages 1–22.

McPhee, M. G. (2013). Intensification of geostrophic currents in the Canada Basin, Arctic Ocean. *Journal of Climate*, 26(10):3130–3138.

Meneghello, G., Marshall, J., Cole, S. T., and Timmermans, M. L. (2017). Observational inferences of lateral eddy diffusivity in the halocline of the Beaufort Gyre. *Under review*.

Proshutinsky, A., Krishfield, R., Timmermans, M.-l., Toole, J., Carmack, E., Mclaughlin, F., Williams, W. J., Zimmermann, S., Itoh, M., and Shimada, K. (2009). Beaufort Gyre freshwater reservoir : State and variability from observations. *Journal of Geophysical Research*, 114:1–25.

Timmermans, M. L., Marshall, J., Proshutinsky, A., and Scott, J. (2017). Seasonally derived components of the Canada Basin halocline. *Geophysical Research Letters*, 44(10):5008–5015.

Tschudi, M., Fowler, C., Maslanik, J. S., and Meier, W. (2016). Polar Pathfinder Daily 25 km EASE-Grid Sea Ice Motion Vectors, Version 3.

Yang, J. (2006). The seasonal variability of the Arctic Ocean Ekman transport and its role in the mixed layer heat and salt fluxes. *Journal of Climate*, 19(20):5366–5387.

Yang, J. (2009). Seasonal and interannual variability of downwelling in the Beaufort Sea. *J Geophys Res*, 114:C00A14.

LIST OF TABLES

	Surface (km^2)	w_{Ek} ($m\,yr^{-1}$)	Vertical flux (Sv)
BGR	989 375	−2.5	−0.077
BGC	85 000	−17.5	−0.047
BGS	95 000	2.0	0.006

TABLE 1. 2003-2012 areal mean Ekman pumping w_{Ek}, and vertical flux for the BGR, BGC and BGS regions, where negative implies downward. Vertical flux is the product of the first two columns.

LIST OF FIGURES

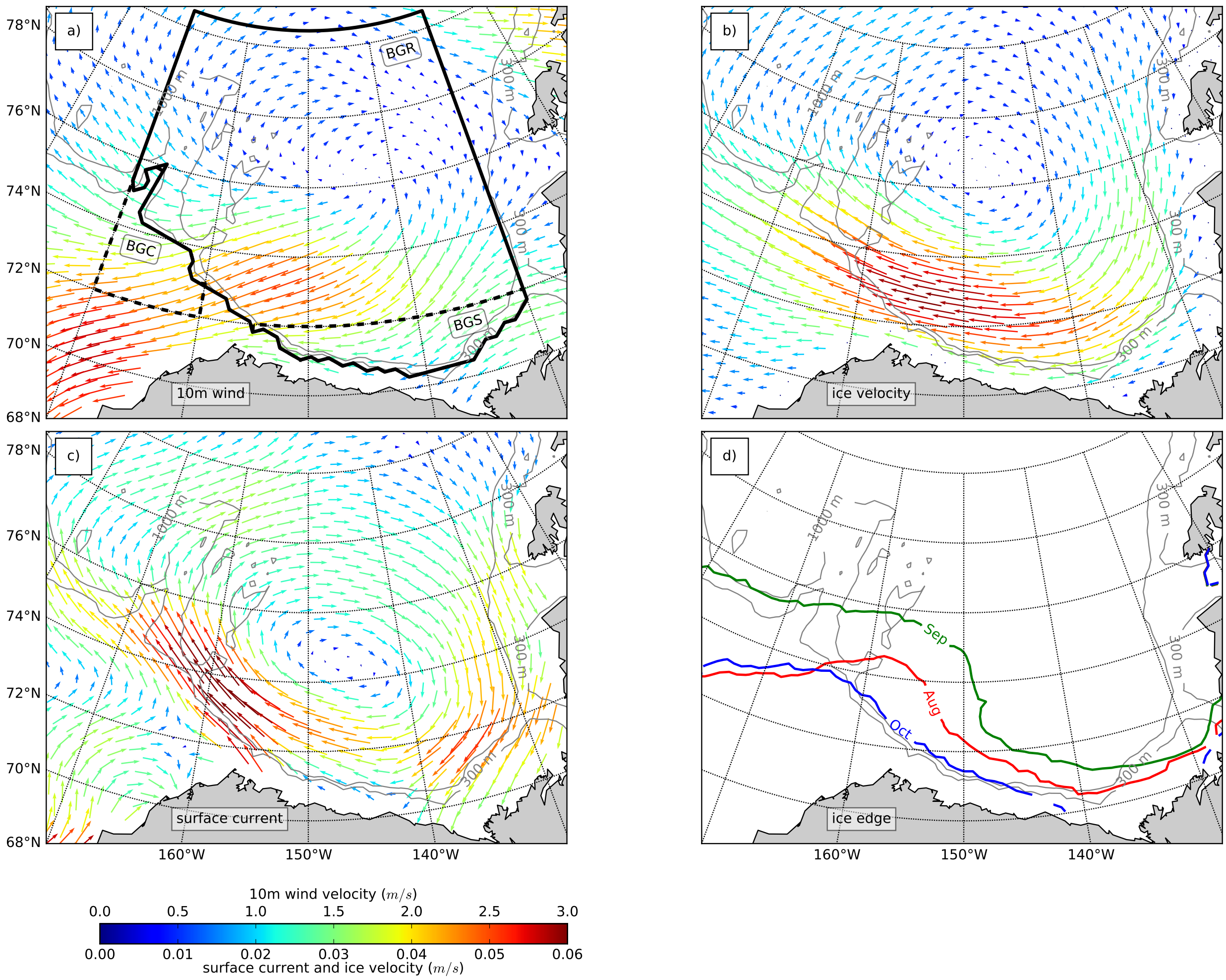

FIG. 1. Ten year means of the four datasets combined to produce estimates of the Ekman pumping field: a) 10 m wind, b) ice velocity, c) surface geostrophic current and d) ice edge (15% ice concentration) for August, September, and October (the ice concentration is larger than 15% everywhere for the rest of the year). The thick black line delimits the Beaufort Gyre Region (BGR); while dashed lines delimit the Beufort Gyre Chukchi Sea in the south-west (BGC) and the Beaufort Gyre Southern regions of the BGR (BGS).

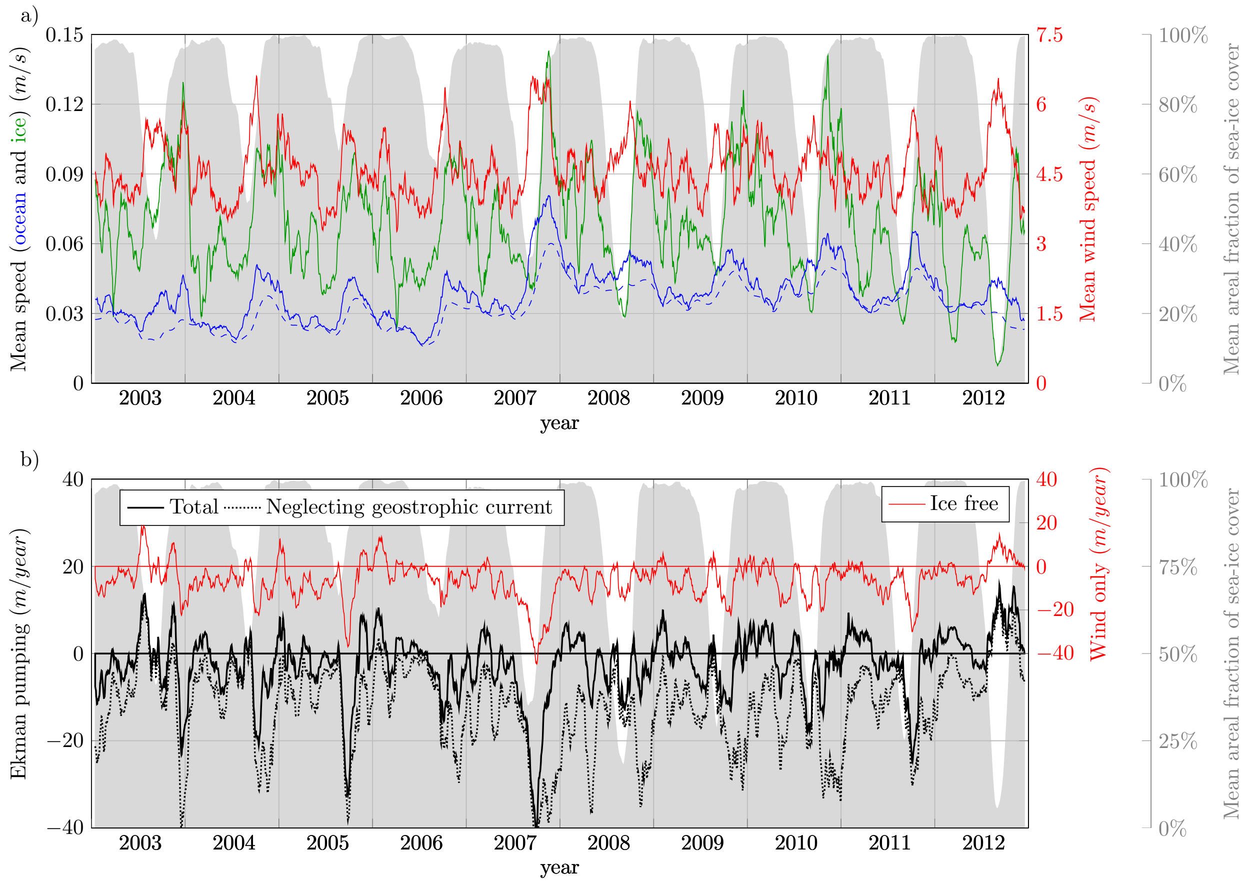

FIG. 2. (a) Thirty-day running mean of 10 m wind velocity $\boldsymbol{u}_a$ (red), ice velocity $\boldsymbol{u}_i$ (green), surface geostrophic current velocity $\boldsymbol{u}_g$ (dashed blue), surface ocean velocity $\boldsymbol{u}_g + \boldsymbol{u}_e$ (solid blue), and sea ice concentration α. (b) Thirty-day running mean Ekman pumping (solid black), Ekman pumping in the absence of geostrophic current (dotted black) and Ekman pumping for a completely ice free BGR (red, note axes on the right). Gray areas in both panels show ice concentration.

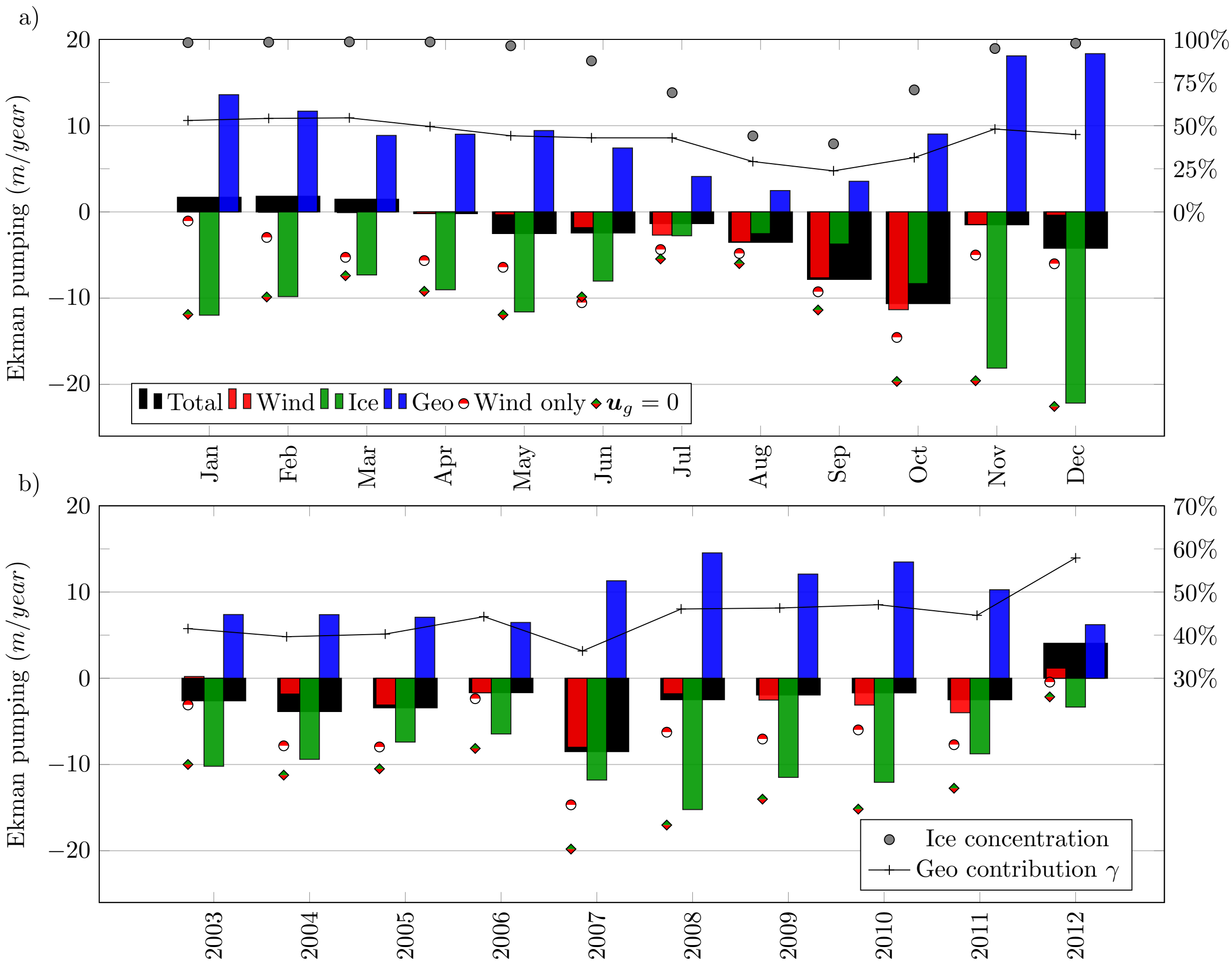

FIG. 3. BGR (Beaufort Gyre Region). Monthly (a) and yearly (b) values, area-averaged over the BGR, of Ekman pumping (black bars) and its three main components: w_a (red bars, pumping over the open ocean), w_{i0} (green bars, pumping in the ice-covered ocean in the absence of a geostrophic current) and w_{ig} (blue bars, modification of under-ice pumping due to ocean currents). The red and green diamonds give the total Ekman pumping $w_a + wi0$ in the absence of an ocean geostrophic contribution. The red and white circles give the wind driven Ekman pumping in a completely ice free BGR. The pumping scale is on the left. The thin black line is a measure of the importance of geostrophic currents given by equation (5) (scale on the right hand side). The gray circles in the top panel (a) indicate the ice concentration α (scale on the right).

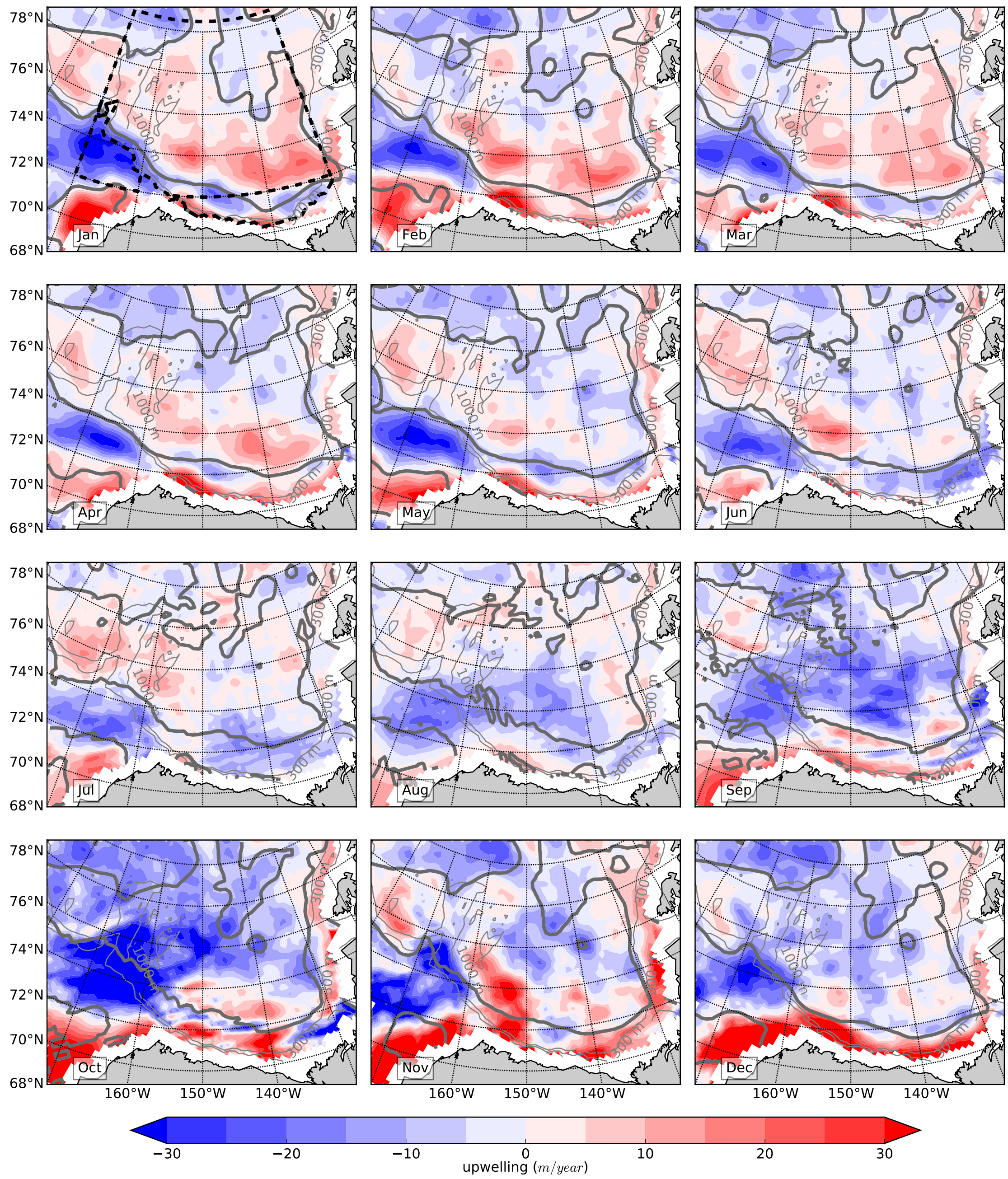

402 FIG. 4. Monthly climatology of Ekman pumping field in $\mathrm{m\,yr^{-1}}$. The black dashed lines denotes the limits of the BGR, BGS and BGC regions — see Figure 1. Gray thick lines mark the location where the geostrophic current component contribution is zero. Interior to this line, the geostrophic current gives an upwelling contribution, outside (e.g., towards the coast in the south) it enhances downwelling.

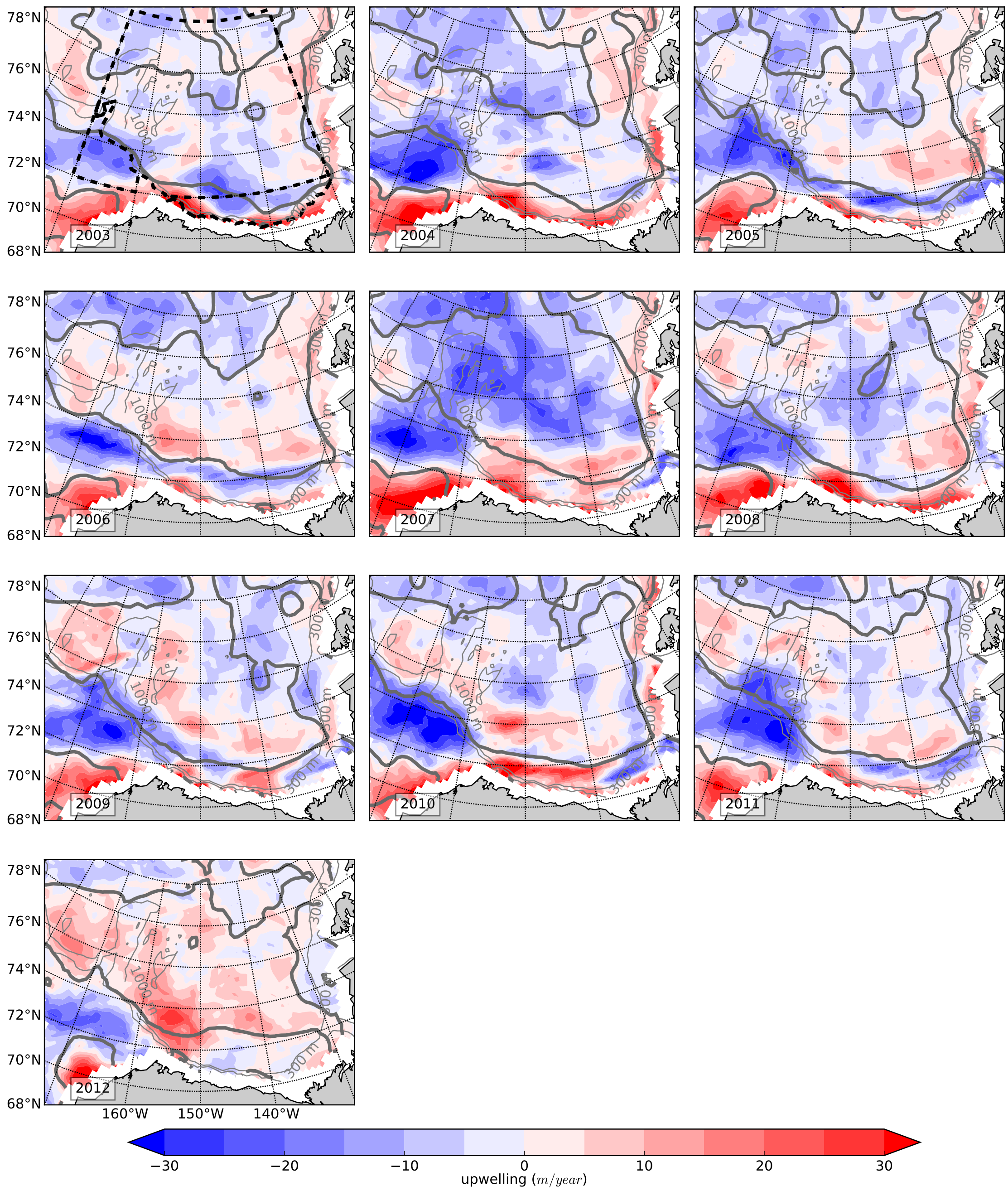

FIG. 5. Yearly climatology of Ekman pumping field in $\mathrm{m\,yr^{-1}}$. The black dashed line denotes the limits of the BGR, BGS and BGC regions — see Figure 1. Gray thick lines mark the location where the geostrophic current component contribution is zero. Interior to this line, the geostrophic current gives an upwelling contribution, outside (e.g., towards the coast in the south) it enhances downwelling

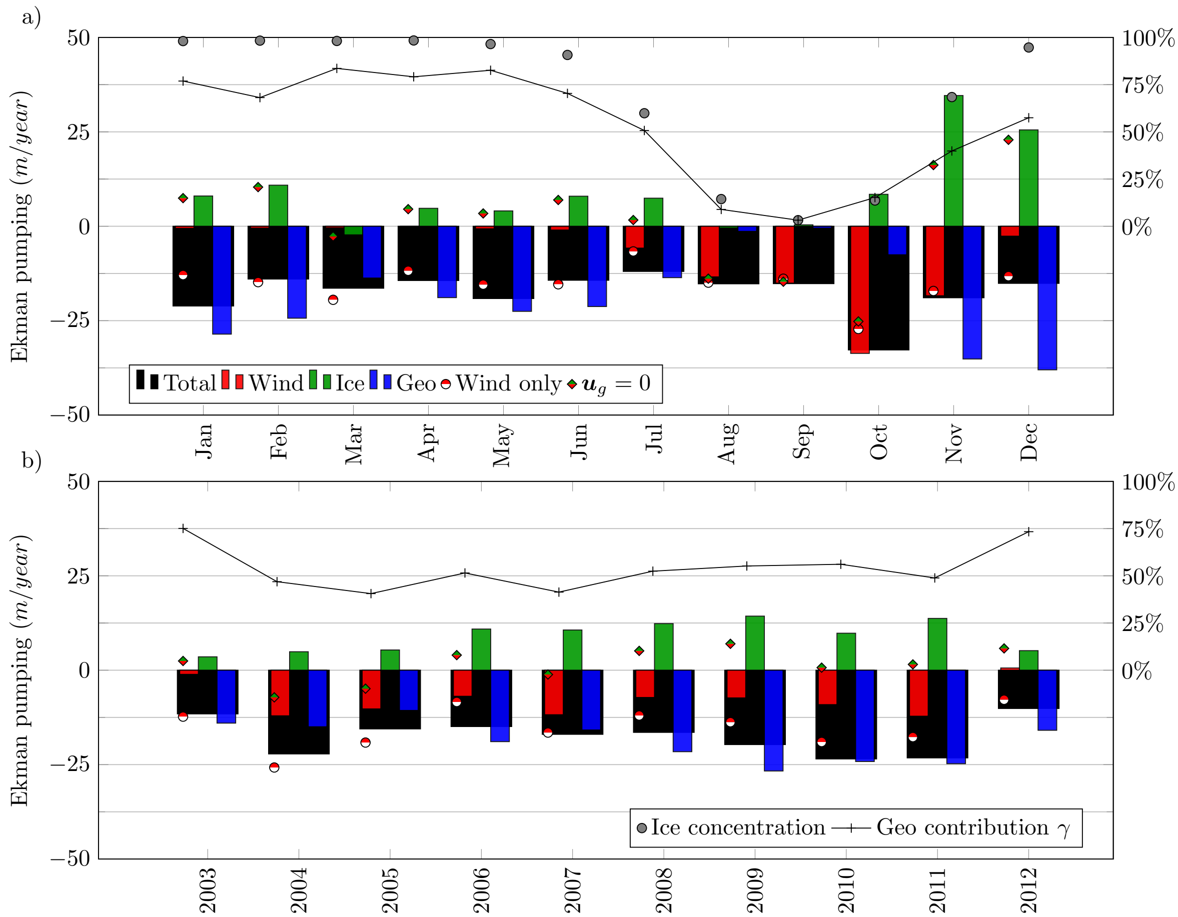

FIG. 6. Area-averaged values over the BGC of (a) Monthly (a) and (b) yearly climatologies of Ekman pumping (black bars) and its three components w_a (red bars, the pumping over the open ocean), w_{i0} (green bars, the pumping in the ice covered ocean in the absence of geostrophic current) and w_{ig} (blue bars, modification of the under-ice pumping due to the geostrophic ocean current). The red and green diamonds give the total Ekman pumping $w_a + wi0$ in the absence of the ocean geostrophic contribution. The red and white circles give the wind-driven Ekman pumping in a (hypothetical) completely ice-free BGR. The pumping scale is on the left. The thin black line is a measure of the importance of geostrophic currents given by equation (5) (scale on the right hand side). The gray circles in (a) indicate the ice concentration α (scale on the right).

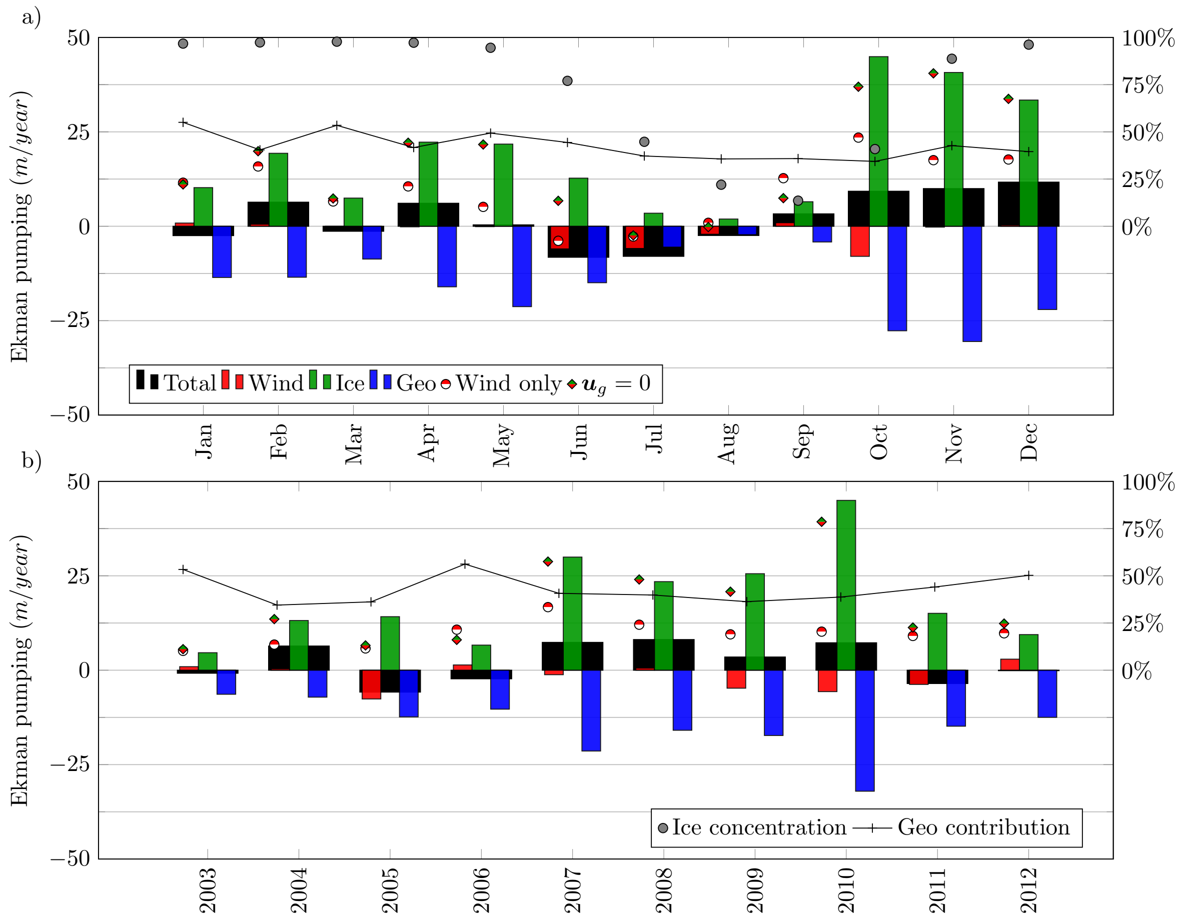

FIG. 7. Area-averaged values over the BGS of (a) Monthly (a) and (b) yearly climatologies of Ekman pumping (black bars) and its three components w_a (red bars, the pumping over the open ocean), w_{i0} (green bars, the pumping in the ice covered ocean in the absence of geostrophic current) and w_{ig} (blue bars, modification of the under-ice pumping due to the geostrophic ocean current). The red and green diamonds give the total Ekman pumping $w_a + wi0$ in the absence of the ocean geostrophic contribution. The red and white circles give the wind-driven Ekman pumping in a (hypothetical) completely ice-free BGR. The pumping scale is on the left. The thin black line is a measure of the importance of geostrophic currents given by equation (5) (scale on the right hand side). The gray circles in (a) indicate the ice concentration α (scale on the right).